HHS Public Access

Author manuscript

*Nat Neurosci*. Author manuscript; available in PMC 2018 June 01.

Published in final edited form as:

*Nat Neurosci*. 2017 December ; 20(12): 1744–1751. doi:10.1038/s41593-017-0004-1.

# Altered cerebellar connectivity in autism spectrum disorders and rescue of autism-related behaviors in mice

**Catherine J. Stoodley**[1,*], **Anila M. D'Mello**[1], **Jacob Ellegood**[2], **Vikram Jakkamsetti**[3], **Pei Liu**[3], **Mary Beth Nebel**[4], **Jennifer M. Gibson**[3], **Elyza Kelly**[3], **Fantao Meng**[3], **Christopher A. Cano**[3], **Juan M. Pascual**[3], **Stewart H. Mostofsky**[4], **Jason P. Lerch**[2], and **Peter T. Tsai**[3,*]

[1]Department of Psychology and Center for Behavioral Neuroscience, American University, Washington DC, USA

[2]Toronto Mouse Imaging Centre, Hospital for Sick Kids, Toronto, Canada

[3]The Department of Neurology and Neurotherapeutics, University of Texas Southwestern Medical Center, Dallas, Texas, USA

[4]Center for Neurodevelopmental and Imaging Research, Kennedy Krieger Institute, Baltimore, Maryland, USA

## Abstract

Cerebellar abnormalities, particularly in Right Crus I (RCrusI), are consistently reported in autism spectrum disorders (ASD). Although RCrusI is functionally connected with ASD-implicated circuits, the contribution of RCrusI dysfunction to ASD remains unclear. Here, neuromodulation of RCrusI in neurotypical humans resulted in altered functional connectivity with the inferior parietal lobule, and children with ASD showed atypical functional connectivity in this circuit. Atypical RCrusI–inferior parietal lobule structural connectivity was also evident in the Purkinje neuron (PN) *TscI* ASD mouse model. Additionally, chemogenetically mediated inhibition of RCrusI PN activity in mice was sufficient to generate ASD-related social, repetitive, and restricted behaviors, while stimulation of RCrusI PNs rescued social impairment in the PN *TscI* ASD mouse model. Together, these studies reveal important roles for RCrusI in ASD-related behaviors. Further, the rescue of social behaviors in an ASD mouse model suggests that investigation of the therapeutic potential of cerebellar neuromodulation in ASD may be warranted.



* peter.tsai@utsouthwestern.edu; stoodley@american.edu.

**Author Contributions**

C.J.S. and P.T.T. formulated human experiments and analysis, while P.T.T. formulated experiments in mice. P.T.T., J.M.G., F.M, and C.C. carried out mouse experiments. A.M.D. and. C.J.S. carried out human studies and analysis. J.E. and J.P.L. performed mouse MRI and analysis. C.J.S., A.M.D., M.B.N., and S.H.M. designed the human ASD analysis, and S.H.M. and M.B.N. provided the human ASD data. V.J., P.L., E.K., and J.M.P. performed electrophysiology experiments and analysis. C.J.S., A.M.D., and P.T.T. prepared the manuscript.

**COMPETING FINANCIAL INTERESTS**

The authors declare no competing financial interests.

ASDs are prevalent neurodevelopmental disorders characterized by social impairment, and repetitive and restricted behaviors[1]. For the past 30 years, the cerebellum has been implicated in the pathogenesis of these disorders. Cerebellar abnormalities are amongst the most consistent findings in postmortem studies of individuals with ASD[2,3], and cerebellar lesions are associated with increased rates of autistic behavior[4–6]. We recently demonstrated that disrupted cerebellar PN function was sufficient to generate ASD-related social and repetitive behaviors in a mouse model of tuberous sclerosis complex[7], further supporting a critical role for the cerebellum in the etiology of ASD. However, the contribution of the cerebellum to the pathophysiology of ASD remains poorly understood.

Within the cerebellum, structural and functional differences in specific cerebellar subregions have been associated with ASD[8–10]. In particular, data from human neuroimaging and animal studies converge on cerebellar RCrusI, reporting differences in lobular volume, grey matter density, white matter integrity, functional activation patterns, and functional connectivity in RCrusI of individuals with ASD[2,8,9]. Here, we combine neuroimaging and neuromodulation in both human and animal models to examine a possible role of RCrusI in ASD.

## RCrusI is functionally connected to multiple whole-brain networks in neurotypical adults

We first examined whole-brain seed-to-voxel functional connectivity (FC) from RCrusI in 34 neurotypical participants. Prior to neuromodulation with transcranial direct current stimulation (tDCS), RCrusI exhibited strong functional connectivity with multiple, predominantly left-lateralized supratentorial regions, including superior, medial, and inferior frontal cortices and temporoparietal regions such as the superior and inferior parietal lobule and middle temporal gyrus (Fig. 1a and Supplementary Table 1). RCrusI was anticorrelated with primary somatomotor regions and Heschl's gyrus. These FC patterns reflect known anatomical connections between RCrusI and the cerebral cortex[11,12] and reaffirm the segregation of motor and nonmotor cerebello–cerebral loops[13,14]. By seeding different locations within RCrusI, we were also able to confirm functional connectivity between RCrusI and ASD-relevant networks, including the default mode network and the frontoparietal network, replicating data from Buckner et al in 2011 (Fig. 1b,c) [11]. Given the extensive functional connectivity of RCrusI, the structural and functional abnormalities in RCrusI often reported in ASD could have wide-ranging impacts on the function of multiple, distributed cortical regions implicated in ASD[8].

## Modulation of RCrusI with tDCS alters brain activity and functional connectivity in neurotypical adults

We next examined whether neuromodulation of RCrusI affected the FC in ASD-associated cerebello–cerebral networks. While acquiring fMRI data in neurotypical adults, we concurrently targeted RCrusI with anodal tDCS. Using the combined tDCS-fMRI data, we then assessed the effects of RCrusI modulation on cerebellar blood oxygen level–dependent (BOLD) activation and whole-brain FC. Anodal tDCS depolarizes the resting membrane

potential, and this excitatory effect is thought to increase cerebellar PN activity[15]. We first compared the BOLD activation between our anodal and sham tDCS groups during 20 min of 1.5-mA tDCS administered over the right posterolateral cerebellum. Compared to sham, anodal tDCS resulted in decreased BOLD signal in the right cerebellar nuclei, with the peak signal difference located in the right dentate nucleus (Montreal Neurological Institute (MNI) coordinates: 22, −62, −38; $P=1.04\times10^{-5}$, $k=110$, max T= 4.62; Fig. 1d). This finding is consistent with increased inhibitory PN output from RCrusI to the right cerebellar nuclei as a result of anodal tDCS. To ensure that the effects of tDCS on FC were specific to RCrusI cerebello–cerebral networks, we seeded several control regions for which we did not anticipate modulation of functional connectivity. We confirmed that anodal tDCS had no effect on FC of neighboring lobules in the cerebellum (right lobule VIIIA), left-lateralized cerebellar homologues (left dentate, left CrusI), or the cerebellar soma to motor hand representation in the right anterior lobe (Supplementary Fig. 1).

We next assessed the impact of anodal tDCS on whole-brain FC from RCrusI. During anodal tDCS, we identified decreased FC between RCrusI and the left inferior parietal lobule (IPL) in the anodal tDCS group compared to the sham group (Fig. 1e and Supplementary Table 2). The IPL is an important node in both default and frontoparietal resting-state networks[16,17], has been implicated in social processing and ASD[18], and is anatomically connected to the cerebellum[19]. Moreover, when FC from the left IPL seed was examined, we not only identified the expected, reciprocal decreased FC with RCrusI but also found altered FC between the IPL seed and important nodes of the default mode network (Fig. 1f). Given the increased male:female ratio in autism, we confirmed that there were no effects of sex on these RCrusI–IPL functional connectivity patterns. Within each sex, anodal versus sham tDCS comparisons were statistically significant (*t* tests; anodal versus sham in males, $P=0.025$; in females, $P=0.0002$), and there were no differences between sexes within each group (anodal males versus females, $P=0.86$; shammales versus females, $P=0.42$). Taken together, our human imaging results demonstrate strong FC between RCrusI and supratentorial networks known to be altered in ASD and demonstrate that modulation of these cerebello–cerebral circuits is possible via anodal tDCS targeting RCrusI.

## Modulation of RCrusI reveals RCrusI–IPL functional connectivity in mice

We next aimed to more directly explore a possible functional role of RCrusI in ASD behaviors. To do this, we turned to mouse models, which offer numerous advantages for performing these functional studies. We began by examining whether the RCrusI–cerebral functional connectivity that we identified in our human participants was consistent between mice and humans. As anodal tDCS reliably modulated functional connectivity between RCrusI and the left IPL, we combined DREADDs (designer receptors exclusively activated by designer drugs)[20,21] with in vivo cortical single-unit recordings to examine whether similar functional connectivity existed and could be modulated in mice. We reduced PN firing by injecting an adeno associated virus (AAV) containing a Cre recombinase-dependent inhibitory DREADD (hM4Di) into RCrusI of mice expressing Cre in PNs (Fig. 2a–c and Supplementary Fig. 2). In acute slice preparations, we confirmed that PN firing was inhibited in the presence of the ligand clozapine-N-oxide (CNO) and that this inhibition was restricted to infected PNs (Fig. 2a and Supplementary Fig s. 3 and 4). The observed

frequency of PN activity was consistent with reductions in PN firing rates in zebrin-expressing cerebellar domains[22–24]. To further confirm the efficacy of cerebellar modulation in vivo, we combined the above chemogenetic strategy with single-unit recordings from RCrusI in anesthetized animals (Supplementary Figs. 5 and 6). We first demonstrated that single-unit recordings were recorded from PNs by the presence of both complex spikes and complex-spike-mediated inhibition of simple spikes (Supplementary Fig. 5). Subsequently, upon CNO administration, we identified reduced PN firing in vivo (Supplementary Fig. 6).

To assess the functional impact of our DREADD-mediated inhibition of RCrusI PNs on cerebello–cerebral circuits, we recorded in vivo single-unit firing activity from mouse parietal association cortex, in the region corresponding to human IPL (Fig. 2d–f and Supplementary Fig. 7) [25–27]. Upon isolation of single units, we identified an inverse relationship between cerebellar modulation and contralateral parietal association cortical activity, consistent with known inhibitory output from the cerebellum (Fig. 2e,f and Supplementary Fig. 8) and the results from our human studies (Fig. 1). DREADD-mediated inhibition of RCrusI PNs resulted in increased single-unit firing rates in the contralateral parietal association cortex, whereas mock infected controls showed no changes in parietal cortical firing rates (Fig. 2e,f and Supplementary Fig. 9). These data demonstrate functional RCrusI–cerebral functional connectivity in mice, mirroring the RCrusI–IPL circuit identified in our human cohort.

## Disrupted RCrusI–cerebral structural connectivity in an ASD mouse model and functional connectivity in individuals with ASD

Given that RCrusI neuromodulation affected similar cerebello–cerebral circuitry in humans and mice and the evidence linking RCrusI to ASD pathogenesis, we next used neuroimaging (structural covariance MRI) to evaluate whether RCrusI–cerebral structural connectivity was disrupted in a mouse model of ASD, the PN *Tsc1*-mutant mouse[7,28,29]. Compared with control mice, mutant mice exhibited significant differences in structural connectivity between bilateral CrusI and multiple cortical areas (Fig. 3a–e, Supplementary Figs. 10 and 11, and Supplementary Table 3). In particular, we identified significant increases in structural connectivity between RCrusI white matter and parietal association areas (Fig. 3e and Supplementary Table 3), suggesting that the RCrusI–IPL functional connectivity identified in human participants and mice is structurally altered in a mouse model of ASD (Figs. 1 and 2). We then examined CrusI–cerebral structural connectivity and identified abnormal, asymmetric structural connectivity between right and left CrusI and contralateral cerebral cortices in mutant mice (Supplementary Figs. 10 and 11).

To determine whether alterations in cerebello–cerebral connectivity are present in individuals with ASD, we also examined RCrusI–left IPL functional connectivity in a large sample of children with ASD (Supplementary Table 4). Compared to age -matched typically developing children, children with ASD showed increased FC between RCrusI and left IPL ($P \simeq 0.012$; Fig. 3f). Taken together, these data demonstrated disrupted RCrusI–cerebral structural connectivity in the *Tsc1*-mutant mouse model of ASD and functional connectivity in human individuals with ASD.

## RCrusI inhibition results in autism-related behaviors in mice

As these findings further indicated that RCrusI abnormalities are relevant to ASD, we next assessed whether RCrusI dysfunction could itself be sufficient to generate ASD-related behaviors. Because clinical studies and our previous work found reductions in PN firing properties and excitability in humans with ASD[30.31] and in an ASD mouse model [7], we evaluated whether chemogenetically mediated inhibition (hM4Di DREADD) of PN firing in RCrusI would be sufficient to generate ASD-related behaviors, such as social impairments, cognitive inflexibility, and repetitive behaviors. We first assessed whether RCrusI inhibition resulted in impairments in social interaction in the three-chambered apparatus (Fig. 4a; $n$ >10 animals for all behavioral tests, except when otherwise specified; all numbers and statistics for behavioral testing are provided in Supplementary Tables 5 and 6)[32]. On social approach testing, vehicle (VEH)-treated mice showed the expected social preference for the novel animal (Fig. 4b, Supplementary Fig. 12 and Supplementary Table 5). However, upon CNO-induced inhibition of RCrusI PN activity, mice demonstrated impaired social preference, supporting a role for RCrusI in the regulation of typical social behaviors (Fig. 4b and Supplementary Fig. 12). To control for the effects of CNO, we examined VEH-and CNO -treated mice injected with GFP into RCrusI and found no social impairment in these mice (Fig. 4b, Supplementary Fig. 12 and Supplementary Table 5).

We then evaluated these animals in a social-novelty model in the three-chambered apparatus. Whereas control mice (VEH-treated RCrusI hM4Di-infected or GFP-infected mice) displayed significant preferences for social novelty, mice with DREADD-mediated inhibition of RCrusI PNs failed to show preference for social novelty (Fig. 4c and Supplementary Fig. 13). Social approach and novelty experiments were repeated in an independent cohort of mice ($n$ =9), who also displayed social deficits upon DREADD-mediated inhibition of RCrusI (Supplementary Figs. 12 and 13).

To ensure that significant alterations in gross motor function did not preclude interpretation of social deficits in RCrusI-inhibited mice, we tested locomotor activity and motor function following CrusI-mediated inhibition. Compared with controls, during testing in the three-chambered apparatus, open field, elevated plus maze, accelerating rotarod, or rhythmic licking paradigms, RCrusI-inhibited mice did not show any observed, significant changes in locomotor activity, anxiety behaviors, or gross motor function that would preclude the interpretation of ASD-related behaviors (Supplementary Figs. 14–17; all statistics are included in detail in Supplementary Table 5). In addition, in light–dark box testing, there was no evidence of visual deficits as a result of RCrusI PN inhibition (Supplementary Fig. 18). We also examined olfactory function and found no deficits in olfaction to nonsocial cues; however, consistent with the social deficits evident in the three-chambered apparatus, DREADD-mediated inhibition of RCrusI led to reduced exploration of social olfactory cues (Supplementary Fig. 18).

Lastly, we tested whether RCrusI might also regulate repetitive behaviors and behavioral inflexibility, two additional core features of ASD. In two independent cohorts, inhibition of RCrusI led to increased grooming behaviors (Fig. 4d and Supplementary Fig s. 15 and 19) at levels comparable to those seen in a mouse model of ASD, the PN *Tsc1*-mutant mouse[7].

RCrusI inhibition also resulted in behavioral inflexibility as assayed in the water Y-maze. Although DREADD-mediated inhibition of RCrusI did not affect acquisition learning of the escape platform location, it did significantly impair reversal learning when compared to control groups (Fig. 4e and Supplementary Fig. 15).

Across behavioral assays, ASD-related behavioral deficits appeared to be specific to inhibition of RCrusI. Social function was not impaired after DREADD-mediated inhibition of left Crus I (LCrusI; Fig. 4b,c and Supplementary Figs. 12, 13, and 20). In addition, LCrusI inhibition did not produce an increase in repetitive or inflexible behaviors (Fig. 4d,e and Supplementary Fig. 15). These findings are consistent with those from human studies, indicating that RCrusI, but not LCrusI, shows converging structural differences in ASD[8]. Taken together, our findings indicate that chemogenetically mediated inhibition of RCrusI is sufficient to generate autism-related behaviors.

## Stimulating RCrusI activity rescues social impairment in PN *Tsc1*-mutant mice

Knowledge of the anatomical substrates underlying behaviors observed in autism carries the potential for remediation and even rescue of these behaviors. Therefore, we evaluated whether modulation of RCrusI function could rescue autistic-related behaviors in a mouse model of ASD (PN *Tsc1*-mutant mice). Given that PN firing rates and excitability are reduced in PN *Tsc1*-mutant mice[7] and that DRE ADD-mediated RCrusI inhibition resulted in social deficits, repetitive behaviors, and inflexible behaviors, we tested whether DREADD-mediated increases in RCrusI PN activity could ameliorate autistic-related behaviors in the *Tsc1* mouse model. To stimulate RCrusI PNs, we injected AAV8 containing the stimulatory DREADD (hM3Dq) into RCrusI of PN *Tsc1*-mutant mice. In acute brain slice recordings, CNO application increased PN firing rates in hM3Gq-containing mutants (Fig. 5a). To determine whether DREADD activation would modify the same RCrusI–parietal lobe circuits that we identified in our human and mouse studies, we attained single-unit in vivo recordings from contralateral parietal association areas. Consistent with our previous findings, activation of RCrusI PNs reduced single -unit firing rates in the left parietal association cortex (Fig. 5b,c), providing further support for the RCrusI–parietal connectivity identified above in our mouse models and human cohorts.

We then evaluated whether stimulation of RCrusI PNs was sufficient to ameliorate the autism-related behaviors seen in PN *Tsc1*-mutant mice. First, we examined social behaviors in these mice in the three-chambered apparatus. In social approach testing, as expected, GFP-infected and VEH-treated, DREADD-infected mutant mice demonstrated impaired social interaction (Fig. 5d and Supplementary Figs. 21 and 22). In contrast, stimulation of RCrusI PNs in mutant mice resulted in significant preference for the social stimulus ($P < 0.0001$), consistent with rescue of social impairments (Fig. 5d and Supplementary Fig. 21). Social novelty testing revealed a similar effect of DREADD-mediated RCrusI stimulation, resulting in a preference for social novelty (Fig. 5e and Supplementary Fig. 22), while GFP-injected or VEH-treated mutant mice demonstrated continued absence of social preference. We again evaluated whether impaired motor coordination or locomotor deficits could have

impacted performance on these social tasks, and we found no differences in motor learning or locomotor function in the accelerating rotarod, elevated plus maze, open field, or three-chambered apparatus between the groups (Supplementary Figs. 23–25). The rescue of social behaviors was specific to RCrusI stimulation, as LCrusI stimulation did not rescue social behaviors (Supplementary Figs. 21 and 22). Finally, we evaluated whether stimulation of RCrusI PN activity in mutant mice might also ameliorate repetitive behaviors and behavioral inflexibility in this ASD model. Unlike social behaviors, DREADD-mediated RCrusI PN stimulation did not rescue increased grooming or behavioral inflexibility as measured in the water Y-maze in PN *Tsc1*-mutant mice (Fig. 5f,g and Supplementary Fig. 24).

## DISCUSSION

Human clinical data and animal models of ASD consistently implicate the cerebellum in the pathogenesis of ASD[2–11]. Previous studies in mouse models have shown that cerebellar dysfunction is sufficient to generate autism-related behaviors in mice [7,23,33,34] but have not examined the specific cerebellar regions responsible for these functions. While differences in RCrusI are strongly associated with ASD, the contribution of RCrusI dysfunction to ASD remains unclear. Here we investigated the role of RCrusI in autism and autism-related behaviors using a multimodal approach (neuromodulation, neuroimaging, and electrophysiology) in both humans and mice, which enabled us not only to examine RCrusI–cerebral cortical circuits, but also to determine the contribution of RCrusI to ASD-related behaviors. We demonstrated that RCrusI is functionally connected to resting-state networks known to be altered in ASD, and identified disrupted RCrusI–cerebral cortical functional connectivity in children with ASD and structural connectivity in the PN *Tsc1* ASD mouse model. Further studies are needed to examine whether these alterations are associated with specific phenotypic presentations of ASD.

In both humans and mice, modulation of RCrusI altered functional connectivity with the IPL, and we observed abnormal functional connectivity between RCrusI and left IPL in individuals with ASD and atypical RCrusI–IPL structural connectivity in the PN *Tsc1*–mutant model of ASD. The left IPL is believed to integrate visuospatial, motor, and cognitive information[35], and it has been shown to be critical for imitating and interpreting the gestures of others[36]. These functions are consistent with evidence that children with ASD struggle to efficiently integrate visual information to guide skilled behaviors[37,38], which is necessary for both imitation and normal social interaction and may be critical to the development of core ASD symptoms[39,40]. Subsequent studies should determine whether the ASD-related behavioral changes observed in mice following RCrusI neuromodulation are mediated by RCrusI–IPL connections.

Our previous work in humans with ASD found that greymatter volume in RCrusI correlates with core ASD symptoms of social and communication skills and repetitive and restricted behaviors[8]. In our current mouse studies, chemogenetically mediated inhibition of RCrusI was sufficient to generate social impairments and repetitive and inflexible behaviors, while excitation of this same region, even in adult *Tsc1*-mutant mice, restored normal social behaviors. These findings point to a role for cerebellar RCrusI in the regulation of these behaviors in mice. In the future, studies should examine whether dysfunction or damage

specific to RCrusI is associated with a higher degree of social impairment and repetitive behavior in other neurodevelopmental and clinical cerebellar populations[41]. Indeed, activation in RCrusI has been associated with a range of tasks relevant to social processing in typically developing individuals, including abstract mentalizing[42], imitation[43], ascribing social attributes to inanimate objects[44], and facial processing[45]. While we did not assess the impact of cerebellar neuromodulation on social processing in humans in this study, our mouse data and human functional connectivity findings suggest that this may be a fruitful direction for future research.

While inhibition of RCrusI resulted in social impairments and repetitive behaviors, RCrusI activation only rescued social impairments and did not rescue repetitive or inflexible behaviors. This discrepancy may reflect the possible involvement of multiple cerebellar areas in the regulation of repetitive, restricted behaviors[10]. Alternatively, it may reflect the existence of differential critical periods for the rescue of social versus repetitive and inflexible behaviors[46]. Future studies will be necessary to determine the specific networks that mediate RCrusI regulation of ASD-related behaviors. These studies will allow us not only to better understand the lateralized nature of these connections but will also further define the functional roles of individual circuit components and mechanisms underlying potential critical periods for treatment of specific ASD-related behaviors.

In addition, because of the established role of the cerebellum in motor control, it was crucial for us to confirm that the observed social impairments and increased repetitive behaviors produced by RCrusI inhibition were not due to motor coordination deficits that would preclude interpretation of ASD-related behavioral testing. Although we did not identify any such locomotor deficits, we cannot exclude a role for RCrusI in motor function. In fact, it is possible that, although this degree of PN RCrusI inhibition was sufficient to generate ASD-related behaviors, it may have been insufficient to generate previously demonstrated motor deficits[47].

Our rescue of social impairments with RCrusI modulation suggests that similar strategies might have the potential to provide therapeutic benefit in individuals with ASD[48]. However, in the current study, as neuromodulation was not conducted in an ASD population, we are unable to assess whether cerebellar neuromodulation will ameliorate ASD behaviors in humans or be tolerated in individuals with ASD. That said, cerebellar neuromodulation has shown promise in the treatment of other neuropsychiatric disorders, such as epilepsy and schizophrenia [15,49]. Here we show that cerebellar neuromodulation via tDCS alters RCrusI–cerebral circuits in neurotypical adults and that functional connectivity in these circuits is atypical in children with ASD. Future studies must examine whether RCrusI modulation in humans mirrors the behavioral benefits seen here in an ASD mouse model. These strategies are of critical importance, as currently there are no therapies for individuals with ASD that target known neurobiological correlates of the disorder. Our findings may thus provide the foundation for future development of neuroanatomically based therapies to improve core symptoms in individuals with ASD.

# ONLINE METHODS

## Participants in the tDCS–fMRI study

Thirty-five participants (23 females, 12 males; mean age 23.79 ± 2.71 years) took part in this study. The study was approved by the Georgetown University Medical Center Institutional Review Board. All participants provided written informed consent and were compensated for their time. Participants were all right-handed, native English speakers with no history of neurological conditions, head trauma, psychiatric or developmental disorders, and no contraindications for tDCS or MRI. Participants were randomly assigned to either the anodal ($n$ =20; 6 males) or sham ($n$ =15; 6 males) tDCS group upon arrival at the scanning center. We prioritized assignment of participants to the active tDCS condition. No statistical methods were used to predetermine sample sizes, but our sample sizes exceed those reported in previous similar studies[50]. Participants were blind to their tDCS condition (active or sham). We excluded one subject from all imaging analyses due to the presence of scanner artifact unrelated to the current experiment, leaving a final sample of 34 participants (23 females, 11 males; mean age 23.75 ± 2.74 years; $n$ =19 anodal (5 males), $n$ =15 sham (6 males)). We also excluded one additional participant from the during-tDCS analyses due to scanner malfunction during tDCS data collection (during tDCS, $n$ =33; 22 females, 11 males; mean age 23.82 ± 2.76 years; $n$= 18 in the anodal group (5 males) and $n$ =15 in the sham group (6 males)).

## Participants with autism spectrum disorder

To examine functional connectivity in a group of participants with autism spectrum disorder (ASD), we analyzed resting-state functional magnetic resonance imaging (rsfMRI) scans collected from children aged 8–13 years old. Eighty-one children had a diagnosis of ASD (mean age 10.36 ±1.44), and 81 were typically developing (TD) children (mean age 10.39 ±1.17) drawn from a larger sample of 195 TD children with usable rsfMRI data (Supplementary Table 4). No statistical methods were used to predetermine sample sizes, but our sample sizes are substantially larger than those reported in previous publications[25]. Data were acquired as part of an ongoing study at the Center for Neurodevelopmental and Imaging Research (CNIR) at the Kennedy Krieger Institute (KKI).

Participants were recruited via advertisements posted in the community, local pediatricians' and psychologists' offices, local schools, social service organizations, chapters of the Autism Society of America, the Interactive Autism Network (IAN) database, outpatient clinics at Kennedy Krieger Institute, and word of mouth. The study was approved by the Johns Hopkins Medical Institutional Review Board. Written consent was obtained from a parent/guardian and assent was obtained from the child. All of the participants had a full scale intelligence quotient of at least 80 as measured by the Wechsler Intelligence Scale for Children version IV ($n$ =148; WISC -IV[51]) or version 5 ($n$ =14; WISC-V[52]), unless there was a 12-point or greater discrepancy in subscale scores, in which case the Verbal Comprehension Index, Perceptual Reasoning Index, or the Visual Spatial Index or Fluid Reasoning Index had to be at least 80 and the lower of the indices could not be below 65. None of the participants had a history of seizures or other neurological disorders, severe chronic medical disorder, diagnosed genetic disorders, or psychotic disorders. TD children

were excluded if they had a first-degree relative with ASD or if parent responses revealed a history of a developmental or psychiatric disorder.

To confirm ASD diagnosis, a Master's level or higher research-reliable psychologist administered the Autism Diagnostic Interview-Revised (ADI-R) and the Autism Diagnostic Observation Schedule–Generic module 3 (ADOS-G, $n$ =35) or the Autism Diagnostic Observation Schedule–2 module 3 (ADOS-2, $n$ =46). All subjects met DSM -IV criteria for ASD based on the ADOS or ADI-R and the judgment of a clinician. Mean scores for the ADOS Social Interaction + Communication, Repetitive Behaviors, and ADOS Total were 11.42 ±3.39, 2.70 ±1.73, and 14.11 ± 3.88, respectively. For the ADI, scores for the Reciprocal Social Interaction, Communication, and Restricted, Repetitive, and Stereotyped Behavior subscales were 20.2 ±5.5, 15.8 ±4.5, and 6.07 ± 2.04, respectively (Supplementary Table 4).

### Combined tDCS–fMRI

TDCS was applied using the NeuroConn DC-Stimulator MR Plus (Jali Medical, Inc.), which is compatible with the MRI environment. Elect rode placement on the head took place outside of the scanner. A 5× 7-cm saline-soaked electrode pad was placed over the right posterolateral cerebellum, 1 cm down and 4 cm to the right of the inion (estimated to be over right lobule VII), with the reference electrode on the right pectoral muscle. Anodal current was ramped up to 1.5 mA over 15 s, applied for 20 min, and then ramped down over 15 s. In sham conditions, the current was ramped up over 15 s and immediately ramped down at the beginning of the 20 min. This allowed participants to experience the initial tingling sensation associated with tDCS without receiving enough stimulation to modulate neuronal excitability. Following the scanning session, participants completed a self-scored questionnaire to rate side effects both during and after tDCS, such as tingling, itching, burning, attention, fatigue, and pain.

### MRI acquisition and parameters

Functional MRI was performed on Georgetown University's Center for Functional and Molecular Imaging (CMFI) Magnetom Trio 3T scanner with a 12-channel head coil. Prior to acquisition of resting-state scans and tDCS, we acquired one high-resolution T1-weighted structural scan (parameters: sagittal acquisition, TR/TE: 1,900 ms/2.52 ms, FoV 250, 1 -mm thickness with 18% oversampling, creating 1-mm cubic voxels). Resting-state scans were acquired prior to (168 volumes, 7 min total) and during (480 volumes, 20 min total) the administration of tDCS (parameters: echo planar imaging (EPI), 38 slices, TR/TE 2,000 ms/30 ms, FoV 64 ×64 mm, 3.2 -mm cubic voxels). For pre-tDCS resting-state scan acquisition, participants were instructed to close their eyes and clear their heads of any thoughts in particular. During the 20 min of tDCS administration, participants passively watched a film while lying still in the scanner.

### Pediatric rsfMRI image acquisition

RsfMRI scans were acquired on a Phillips 3T MRI scanner (Achieva, Philips Healthcare, Best, The Netherlands) using a single-shot, partially parallel (SENSE) gradient-recalled echo planar sequence (parameters: TR/TE: 2,500 ms/30 ms, flip angle = 70°, SENSE

acceleration factor of 2, 3-mm axial slices with no slice gap and an in-plane resolution of 3.05 × 3.15 mm (84 ×81 voxels), 128 or 156 timepoints) and either an 8-channel ($n$ =112) or a 32 -channel head coil ($n$ = 50). An ascending slice order was used, and the first four volumes (10 s) were discarded at acquisition to allow for magnetization stabilization. Children were instructed to relax and focus on a crosshair while remaining as still as possible.

### Resting-state functional connectivity analysis in healthy adults

Image preprocessing and statistical modeling were carried out using the CONN toolbox (version 15e) as implemented in Matlab 2015 (http://www.nitrc.org/projects/conn)[53]. For each participant, resting-state functional scans were preprocessed using a standard pipeline: removal of the first five volumes, slice-time correction, realignment and unwarping, ART scrubbing for outlier detection using the default thresholds in CONN, normalization, and smoothing (8 mm FWHM). Images were bandpass-filtered (0.01–0.09 Hz) and confounds such as signal from white matter, cerebrospinal fluid (CSF), movement parameters, and time-series predictors of global signal were removed following the CompCor strategy implemented in the CONN toolbox[54]. Groups did not significantly differ in maximum head displacement during tDCS ($t$ test, $P$= 0.27) or average number of scans removed ($t$ test, $P$= 0.11). Whole-brain BOLD signal was not used as a regressor to enable interpretations of anticorrelations. We conducted seed-to-voxel analyses from a priori regions of interest (ROIs). For each ROI, whole-brain seed-to-voxel analyses were conducted to identify voxels with highly correlated time-courses. BOLD-signal time-series were extracted from each seed and correlated with every other voxel in the brain using the CONN toolbox. At the first level, seed-to-voxel correlation maps were created for each participant both before and during -tDCS. We conducted functional connectivity analysis on the 20 min of data collected during tDCS. Functional connectivity maps were compared between groups using two-tailed $t$ tests (anodal > sham and s ham > anodal). Data distribution was assumed to be normal, but this was not formally tested. Results were thresholded at $P$ < 0.001 at the voxel level, with a false discovery rate (FDR) cluster correction of $P$ <0.05.

### Resting-state functional connectivity analysis in ASD participants

Data were processed using Statistical Parametric Mapping software (SPM12, Wellcome Trust Centre for Neuroimaging, Department of Cognitive Neurology, Cambridge, UK) and custom code written in Matlab (Mathworks, Inc.). RsfMRI scans were slice time adjusted, realigned, and normalized to the Montreal Neurological Institute template, and each rsfMRI scan was temporally detrended on a voxel-wise basis. The CompCor strategy was used to estimate spatially coherent noise components from tissues not expected to exhibit BOLD signals and remove them from the data, as this method has been shown to selectively attenuate physiological noise and motion artifact[54,55]. RsfMRI data were smoothed (6-mm FWHM) and bandpass-filtered (0.01–0.1 Hz). Using ROIs defined by our tDCS–fMRI data (RCrusI, L IPL), we conducted an ROI-to-ROI analysis to assess whether FC between these regions was disrupted in children with ASD. For each subject, average time-series were extracted from each ROI; a pairwise Pearson correlation was calculated and converted to a $z$-score representing RCrusI–L LIPL functional connectivity using Fisher's $z$-transform.

We matched the distribution of demographic (age, gender, handedness, intellectual ability derived from WISC-IV/WISC-5, and socioeconomic status[56]; Supplementary Table 4) and rsfMRI data quality covariates (mean FD, receiving coil type, scan length) in the ASD and TD groups. Because of the large number of covariates, we used the MatchIt package in R[57] to calculate a propensity score for each subject and find 81 ASD–TD pairs with the smallest distance between them to minimize selection bias[58]. Supplementary Table 4 summarizes the characteristics of the final sample. Data distribution was assumed to be normal, but this was not formally tested. We compared RCrusI–L IPL functional connectivity between groups using a two-sample *t* test thresholded at $P < 0.05$.

## Seed selection

To investigate functional connectivity changes from the cerebellar region under the active electrode, the SUIT atlas[59,60] was used to create an RCrusI seed (consisting of the whole volume of RCrusI). To examine cerebello–cerebral connectivity in various resting-state networks, spherical seeds were created using peak coordinates from Buckner et al.[11]. Buckner and colleagues explored the organization of cerebello–cerebral networks using resting-state functional connectivity, finding that the cerebellum houses multiple representations of the seven major cerebral resting state networks. RCrusI of the cerebellum primarily targets two cerebral resting-state networks: the default mode network (DMN) and the frontoparietal (FP; also known as the cognitive control) network. The size of the seeds reflected the size differences in the territories of these networks in the cerebellum. Within RCrusI, the frontoparietal network seed was a 5-mm sphere centered on MNI coordinates 39, −72, −27[11], and the DMN seed was an 8-mm sphere centered on MNI 29, −78, −32. The seeds were visually checked to ensure that they did not overlap and to confirm that both were contained within RCrusI. To determine that the effects of tDCS were specific to the right cerebellar hemisphere, we created two left-lateralized region-of-interest seeds (left dentate nucleus; LCrusI) using the SUIT atlas. In addition, to ensure that tDCS modulation was specific to cerebello–cerebral cognitive networks involving RCrusI, we created two motor seeds: one 5-mm spherical seed centered on MNI coordinates 17, −52, −24, corresponding to the hand representation in the cerebellar anterior lobe; and a seed in lobule VIIIA, which abuts lobule VII, created using the SUIT atlas. Labeling and localization of regions was conducted using the AAL atlas in MRICron[61] for cortical regions and the SUIT atlas for localization of cerebellar results[59,60].

## BOLD activation during tDCS

Preprocessed resting-state data from the CONN toolbox were entered into SPM to examine BOLD activation patterns in anodal tDCS versus sham groups during tDCS administration. In order to capture small variations in BOLD signal as a result of tDCS administration during rest, we modeled each TR (2.5 s) as a separate onset with a duration of 2.5 s for the duration of tDCS application (20 min) at the first level. ART motion parameters and outliers were entered as regressors. Individual contrast files were then entered into a full factorial model in SPM8. To reflect very small variations in BOLD signal during rest periods, we used an uncorrected threshold of $P < 0.001$ at the voxel level with a minimum cluster size of $k = 150$.

## Mice

*L7/Pcp2-Cre* ($L7^{Cre}$) transgenic mice[62] were attained from Jackson Laboratories. $L7^{cre}$;$Tsc1^{loxP/loxP}$ (mutant) animals were generated by crossing *L7/Pcp2-Cre* ($L7^{Cre}$) transgenic mice with *loxP*-flanked *Tsc1* mice ($Tsc1^{loxP/loxP}$) [63] to yield $L7^{Cre}$;$Tsc1^{loxP/+}$progeny. These progeny were then crossed with one another to ultimately yield $Tsc1^{loxP/loxP}$and $L7^{Cre}$;$Tsc1^{loxP/loxP}$(mutant) mice. These were then used as breeders with $Tsc1^{loxP/loxP}$mice crossed to $L7^{Cre}$;$Tsc1^{loxP/loxP}$mice. Only male animals were used for behavioral experiments. Mice were of mixed genetic backgrounds (C57Bl/6J, 129 SvJae, BALB/cJ). Littermate controls were used for all behavioral experiments. All experimental protocols were approved by the University of Texas Southwestern Institutional Animal Care and Uses Committee.

## Viral injections

Stereotactic injections of virus were done using stereotaxic apparatus (Stoelting) in combination with a nanojector (WPI) 2–3 weeks prior to behavioral testing. Viruses utilized in this study included: AAV8-hSyn-DIO-hM3D(Gq)-mCherry (hM3Dq), AAV8-hSyn-DIO-hM4D(Gi)-mCherry (hM4Di), and AAV8-CMV-GFP, all of which were obtained from University of North Carolina, viral vector core. Injections were targeted to cerebellar domains, RCrusI (stereotactic coordinates from lambda: −3.25, −2.75, −0.8) or LCrusI (stereotactic coordinates from lambda: 3.25, −2.75, −0.8).

## Chemogenetic activation

For in vivo studies, mice were administered clozapine-N-oxide (CNO): 5 mg/kg intraperitoneally 30 min prior to initiation of behavioral testing. CNO (Sigma) was dissolved in 0.5% DMSO in 0.9% saline (vehicle). For in vivo electrophysiology experiments, CNO was administered after baseline recording was attained with continued recording subsequent to CNO administration. For acute slice recordings, CNO studies were performed at 10μM.

## Electrophysiology in acute slices

**Acute slice preparation—**Acute sagittal slices (250–300 μm thick) were prepared from the cerebellum of 4 and 6 week old mutant and control littermates. Slices were cut in an ice-cold artificial cerebrospinal fluid (ACSF) solution consisting of (in mM): 125 NaCl, 26 $NaHCO_3$, 1.25 $NaH_2PO_4$, 2.5 KCl, 1 $MgCl_2$, 2 $CaCl_2$, and 25 glucose (pH 7.3, osmolarity 310), equilibrated with 95% $O_2$ and 5% $CO_2$. Slices were initially incubated at 34°C for 25 min and then at room temperature (21–22°C) prior to recording in the same ACSF.

**Recordings—**Visually guided (infrared DIC videomicroscopy and water-immersion 40×objective) whole-cell recordings were obtained with patch pipettes (2–4 M Ω) pulled from borosilicate capillary glass (World Precision Instruments) with a Sutter P-97 horizontal puller. Electrophysiological recordings were performed at 31–33 ° C. For current-clamp recordings, the internal solution contained (in mM): 150 potassium-gluconate, 3 KCl, 10 HEPES, 0.5 EGTA, 3 MgATP, 0.5 GTP, 5 phosphocreatine-$tris_2$, and 5 phosphocreatine-$Na_2$. The pH was adjusted to 7.2 with NaOH. Current-clamp and extracellular recordings were performed in NBQX (5 μM), R-CPP (2.5 μM), and picrotoxin (20 μM) to block AMPA

receptors, NMDA receptors, and $GABA_A$receptors, respectively. All drugs were purchased from Sigma-Aldrich or Tocris.

**Data acquisition and analysis—**Electrophysiological data were acquired using a Multiclamp 700B amplifier (Axon Instruments), digitized at 20 kHz with either a National Instruments USB-6229 or PCI-MIO 16E-4 board and filtered at 2 kHz. Acquisition was controlled with custom software written in either MATLAB or pCLAMP. Series resistance was monitored in voltage-clamp recordings with a 5-mV hyperpolarizing pulse, and only recordings that remained stable over the period of data collection were used. Glass monopolar electrodes (1–2 MΩ) filled with ACSF in conjunction with a stimulus isolation unit (WPI, A360) were used for extracellular stimulation of climbing and parallel fibers.

## Mouse in vivo electrophysiology

**Acute surgery and recording—**Male and female mice of each genotype aged 5–7 weeks were anesthetized using a combination of ketamine (100 mg/kg), xylazine (10mg/kg), and acepromazine (2mg/kg). The depth of anesthesia was confirmed by an absent reflex withdrawal of the hind paw to a strong pinch. The mouse was transferred to a stereotaxic head mount for surgery. Core body temperature was measured with a rectal probe and maintained at 37°C with a TC-1000 temperature controller (CWE Inc., Ardmore, PA). A craniotomy for access to the parietal cortex was performed to remove a rectangular flap of bone over the recording region. The location of recording was 1.5 mm anterior and 0.75 mm lateral to lambda in the left hemisphere for parietal association cortex recordings. Location of recording was 3 mm posterior and 2.5 mm lateral to lambda in the right hemisphere for RCrusI recordings. Care was taken to avoid surface blood vessels during microelectrode insertion. Tungsten microelectrodes (World Precision Instruments Inc., Sarasota, FL;3 -μm insulation, 0.356-mm shaft, 2 MΩ, 1–2-μm tip) were inserted orthogonal to the parietal cortex surface and advanced to a depth of 450–500μm for recordings. The exposed dura was kept intact during surgery and was moistened with saline throughout the experiment. Electrophysiological activity was acquired, amplified, and filtered (bandpass, 400–20,000 Hz) with a MultiClamp 700B programmable amplifier (Axon Instruments, Molecular Devices, Sunnyvale, CA). CNO was administered intraperitoneally (i.p.) via a 1-mLsyringe and tubing primed with CNO solution prior to i.p. insertion of a winged infusion set to allow injection of the required dose without air bubbles. The winged infusion set (Terumo Corp, Japan;27Gx1/2, 20 cm of tubing) was inserted i.p. prior to insertion of recording electrode. Microelectrodes were left in situ for 10–15 min of baseline activity acquisition, followed by CNO i.p. injection, and data was continuously acquired for 65 min after the CNO injection. Movement of the mouse (and a possible change in location of the electrode within the brain) during CNO i.p. injection was prevented by virtue of (i) having the tubing fixed at multiple points in its length with adhesive tape, (ii) fixing the injecting port to the Faraday cage with adhesive tape, and (iii) having the mouse on a vibration-isolation table (TMC, Peabody, MA), isolated from the Faraday cage so that any miniscule changes in pressure or movement of the injecting port while injecting CNO were not transmitted to the mouse.

For cerebellar recordings, whiskerpad-evoked activity[64] was elicited with two -needle stimulating electrodes, insulated to within the point of entry into the skin, inserted into the

skin between whisker rows A &B (parallel to the long axis of the whisker rows) and C & D along the whole length of the whisker rows. Unipolar biphasic current pulses (2 ms in total duration, 1.9 mA in current pulse amplitude) were administered 15 s apart, for a total of 200 trials. Single-unit electrodes and recording protocols for spontaneous activity were similar to those used for cortical spikes. The electrode was advanced in depth in 10 μm steps orthogonally in CrusI until the characteristic high-firing Purkinje neuron was detected. Further confirmation of the depth of recording was done by observing complex spike suppression of simple spikes as characteristic of the Purkinje neuron layer.

**Data analysis—**Analysis was done offline using programs written in Matlab (Mathworks, Natick, MA). Extracellular multiunit action potentials (spikes) were detected as positive or negative voltage deflections that were 5 times greater than the median absolute deviation of a voltage recording[65–67]. To avoid multiple detections of the same spike, a 'detector dead time'of 1.5 ms followed each spike detection. Spikes were sorted into single units using the Matlab toolbox Wave_Clus[65–67] for semiautomated clustering and sorting of single units.

Cerebellar single-unit sorting for simple spikes was done similarly to that for cortical spikes. Evoked activity was plotted and evoked complex spikes were detected by human eye in a Matlab graphical user interface (GUI) window. Their occurrence time stamps were marked in the GUI and exported for comparison with timestamps of simple spikes.

## Mouse magnetic resonance imaging

A total of 29 male mice were used for these studies. Total numbers included 13 mutant mice and 16 littermate controls. Mice received vehicle treatment starting at 6 weeks of age for a total of 4 weeks. Mice were then perfused with 4% PFA and 2mM multihance (Bracco Imaging, Canada). A multichannel 7.0-Tesla MRI scanner (Agilent Inc., Palo Alto, CA) was used to image the brains, left within their skulls. Sixteen custom-built solenoid coils were used to image the brains in parallel[68].

**Anatomical scan (40 μm)—**Parameters for the anatomical MRI scans were: T2 - weighted, 3D fast spin echo sequence, with a cylindrical acquisition of *k*-space, with a TR of 350 ms, TEs of 12 ms per echo for 6 echoes, field of view of 20 ×20 ×25 $mm^3$, and a matrix size of 504 ×504 ×630, giving an image with 0.040-mm isotropic voxels. Total imaging time was 14 h.

**Registration and deformation-based analysis—**To visualize and compare any differences in the mouse brains, the images were linearly (6 parameter followed by 12 parameter) and nonlinearly registered. All scans were then resampled with appropriate transform and averaged to create a population atlas representing the average anatomy of the study sample. The result of the registration was to deform all scans into exact alignment with each other in an unbiased fashion[69,70]. The Jacobian determinants of the deformation fields were then used as measures of volume at each voxel. Significant volume changes could then be calculated by warping a pre-existing classified MRI atlas onto the population atlas, which allowed a volume of 159 segmented structures encompassing cortical lobes, large white matter structures (i.e., corpus callosum), ventricles, cerebellum, brain stem, and olfactory

bulbs. This atlas built upon the Dorr atlas[71] with additional delineations of the cerebellum according to Steadman et al.[72] and the cortex according to Ullmann et al.[73].

**Anatomical correlations—**Anatomical correlations were used as a measure of connectivity throughout the brain. Strong correlations between two regions in the brain have been taken as a measure of connectivity strength. Brain areas that are highly correlated in size have been demonstrated to be involved in systems that have specific functions[74], such as the grey matter of the hippocampus, which correlates quite strongly with several areas known to be involved in the memory system[75]. This technique (structural covariance/connectivity MRI or scMRI) has been utilized in multiple human studies[74,76–80]. One particular study in the human brain revealed covariance between cortical thickness of Broca's area and that of Wernicke's area across subjects, consistent with anatomic connectivity via the arcuate fasciculus. These findings highlight the information that can be obtained through these anatomical correlations[29]. Initial assessment of the anatomical correlations was targeted to examine the efferent projections from the deep cerebellar nuclei (DCN) based on the DCN projections outlined in *The Mouse Nervous System* by Watson, Paxinos, and Puelles [81]. Statistics are summarized in Supplementary Table 3. Pearson's correlation coefficients were calculated separately and compared for the groups examined. *P* values were all calculated with linear models: CrusI –cortical structure for control and mutant groups individually and CrusI–cortical structure× genotype for the interaction. All calculations were performed in R.

**Software—**All software and code used for mouse MRI analysis and registration is freely available on GitHub (https://github.com/Mouse-Imaging-Centre/). For registration, see https://github.com/Mouse-Imaging-Centre/pydpiper/. For analysis, see https://github.com/Mouse-Imaging-Centre/RMINC/.

## Behavioral analysis

Statistics of behavioral experiments can be found in Supplementary Tables 5 and 6. No statistical methods were used to predetermine sample sizes, but our sample sizes are substantially larger than those reported in previous publications[7]. Behavioral studies were performed according to the following schedule: week one: rotarod; week two: open field, three-chambered apparatus, grooming, elevated plus maze; week three: water Y-maze; week four: olfaction. An additional cohort of mice had light–dark box and rhythmic licking tested during week three. Testing was performed during the morning hours for all behavioral experiments. Animals were group housed under a 12-h:12-h light:dark cycle. Chemogenetic studies involved the following controls: GFP infection (VEH and CNO) and DREADD infection (VEH and CNO) for all behavioral studies to control for DREADD activation, potential effects of vehicle, and CNO off-target effects.

**Social interaction—**Animals were tested for social interaction in the three -chambered apparatus (Nationwide Plastics) as previously described[7,82]. Briefly, animals were individually housed for 30 min before being introduced to the middle chamber of the three-chambered apparatus for 10 min. Animals were then allowed to explore the entire apparatus for 10 min. A novel animal and novel object were then inserted into opposite chambers in

the apparatus and animals were tested for 10 min in this social approach model. Then, a novel animal (male, age-matched, C57BL/6j) was inserted into the chamber with the novel object and social novelty was evaluated for an additional 10 min. Time spent in each chamber and the number of crossings between chambers were recorded in an automated manner (Topscan, CleverSys Inc.). Time spent interacting with the novel animal and object was recorded with a stopwatch by an examiner who was blinded to experimental condition. Animals were tested between 7 and 9 weeks of age. Light at the center of the three chambered apparatus was 30 lux for all experiments. All behavioral assays (including social interaction) were performed by an examiner blinded to genotype.

**Open field—**Open field testing was performed as described for a 15-min period[7,83,84]. Movement and time spent in the center quadrants were recorded by video camera, and automated analysis was performed using Noldus Ethovision software. Light at the center of the open field was 40 lux. Animals were tested between 7 and 9 weeks of age.

**Elevated plus maze—**Elevated plus maze testing was performed as previously described for a 5-min period[7,83]. Distance traveled and time in open arms were recorded by video camera, and automated analysis was performed using Noldus Ethovision software. Light in the open arms was 15 lux. Animals were tested between 7 and 9 weeks of age.

**Grooming—**Animals were removed from home cages and placed individually into new cages containing bedding only. Animals were allowed to habituate to the new cage for 10 min. Animals were then observed for 10 min, and time spent grooming was recorded by an examiner blinded to experimental condition/genotype[7,85]. Animals were tested between 7 and 9 weeks of age.

**Water Y-maze—**Reversal learning was tested using the water Y -maze as described previously[7,83,86]. Briefly, animals were habituated to the apparatus. Then, on trial sessions 1–3, mice were given 15 trials and tasked to locate a submerged platform placed in one of the maze arms. After trial session 3, the platform was moved to the other arm of the Y shaped apparatus. Mice were then tested for three additional sessions with 15 trials/session (reversal trials 1–3). Animals underwent two trial sessions per day. The numbers of correct trials and number of trials required to achieve five consecutive correct trials were recorded. Animals were tested between 9 and 10 weeks of age.

**Olfaction—**Olfaction was tested using the habituation/dishabituation experimental model described and performed previously[7,87]. Briefly, animals were habituated to the testing environment for 30 min, then presented sequentially with cotton swabs dipped in either water, almond extract, or banana extract diluted at 1:200 (McCormick). Mice were exposed to each olfactory stimulus for three trials. Time spent sniffing each olfactory stimulus was recorded.

**Accelerating rotarod—**Animals were tested using the accelerating rotarod as previously described over 5 consecutive days[7,88]. Animals were tested at 6 weeks of age. Latency to fall was recorded.

**Light/dark Box—**Mice were habituated in the dark side of the chamber for 2 min prior to commencement of the 10 min trial. With commencement of each trial, the door between the light and dark boxes was opened and mice were allowed to freely move within the chambers. Data was collected with photobeam tracking software (Medtronic). Light level was 300 lux. Light and dark sides of the apparatus were 25.4 cm ×25.4 cm.

**Licking—**In the week prior to testing, mice were water restricted for 12 h at a time, receiving water at 1-h intervals three times per day during training and acclimation to testing environment. During testing, mice were allowed to habituate to the cage for 20 min without water. Commencement of the test occurred upon addition of the water bottle. The water supply and the bottom of the cage were connected to an A/D converter to create a closed - loop circuit when the mouse drank from the bottle[89]. Data was collected using Gobetwino programming software.

### Immunohistochemistry

Mice were perfused and postfixed with 4% paraformaldehyde. Sections were prepared by cryostat sectioning. Calbindin (Sigma, Cell Signaling) staining for PNs was used for quantification of infection efficiency.

### Statistics

Data are reported as mean ± s.e.m., and statistical analysis was carried out with GraphPad Prism software. One- and two-way ANOVA with *post hoc* Bonferroni multiple -comparison tests were utilized to evaluate significance for behavioral tests. A Life Sciences Reporting Summary is available.

### Data availability

The data that support the findings of this study are available from the corresponding author upon reasonable request.

## Supplementary Material

Refer to Web version on PubMed Central for supplementary material.

## Acknowledgments

A.M.D. and C.J.S. acknowledge the support of P. Turkeltaub, C. Barrett, B. Drury, and S. Martin in neuroimaging data collection and analysis. All neurobehavioral experiments were performed at the Department of Psychiatry Rodent Behavioral Core, and the authors thank the Director for Core services, S. Birnbaum, for her assistance. The authors also appreciate assistance from the UT Southwestern Whole Brain Microscopy Facility, and from B. Nieman and L.Spencer Noakes for their work on the MRI sequence used. P.T.T. acknowledges support from the National Institute of Neurologic Disorders and Stroke of the NIH (K08 NS083733), the Child Neurology Foundation, the Tuberous Sclerosis Alliance, and the University of Texas Southwestern Medical Center Disease Oriented Clinical Scholar Award. C.J.S. acknowledges funding from the National Institute of Mental Health of the NIH (R15 MH106957), pilot research funds from the Department of Psychology, and institutional startup funds from American University. J.P.L and J.E. acknowledge support from the Canadian Institute for Health Research (CIHR) and the Ontario Brain Institute (OBI). S.H.M. acknowledges support from Autism Speaks, the National Institute of Mental Health (R01 MH085328-09, R01 MH078160-07, and K01 MH109766), and the National Institute of Neurological Disorders and Stroke (R01 NS048527-08). E.K. acknowledges funding from National Institute of Drug Abuse T32 training grant (T32 DA007290-24).

## References


1. Wingate M, et al. Prevalence of Autism Spectrum Disorder Among Children Aged 8 Years -Autism and Developmental Disabilities Monitoring Network, 11 Sites, United States, 2010. Mmwr Surveill Summ. 2014; 63
2. Skefos J, et al. Regional alterations in purkinje cell density in patients with autism. PloS one. 2014; 9:e81255. [PubMed: 24586223]
3. Whitney ER, Kemper TL, Bauman ML, Rosene DL, Blatt GJ. Cerebellar Purkinje cells are reduced in a subpopulation of autistic brains: a stereological experiment using calbindin-D28k. Cerebellum. 2008; 7:406–416. DOI: 10.1007/s12311-008-0043-y [PubMed: 18587625]
4. Limperopoulos C, et al. Does cerebellar injury in premature infants contribute to the high prevalence of long-term cognitive, learning, and behavioral disability in survivors? Pediatrics. 2007; 120:584–593. 120/3/584 [pii]. DOI: 10.1542/peds.2007-1041 [PubMed: 17766532]
5. Bolduc ME, Limperopoulos C. Neurodevelopmental outcomes in children with cerebellar malformations: a systematic review. Dev Med Child Neurol. 2009; 51:256–267. DOI: 10.1111/j.1469-8749.2008.03224.x [PubMed: 19191827]
6. Catsman-Berrevoets CE, Aarsen FK. The spectrum of neurobehavioural deficits in the Posterior Fossa Syndrome in children after cerebellar tumour surgery. Cortex. 2010; 46:933–946. DOI: 10.1016/j.cortex.2009.10.007 [PubMed: 20116053]
7. Tsai PT, et al. Autistic -like behaviour and cerebellar dysfunction in Purkinje cell Tsc1 mutant mice. Nature. 2012; 488:647–651. DOI: 10.1038/nature11310 [PubMed: 22763451]
8. D'Mello AM, Crocetti D, Mostofsky SH, Stoodley CJ. Cerebellar gray matter and lobular volumes correlate with core autism symptoms. NeuroImage:Clinical. 2015; 7:631–639. DOI: 10.1016/j.nicl.2015.02.007 [PubMed: 25844317]
9. D'Mello AM, Stoodley CJ. Cerebro-cerebellar circuits in autism spectrum disorder. Front Neurosci. 2015; 9:408. [PubMed: 26594140]
10. Mosconi MW, Wang Z, Schmitt LM, Tsai P, Sweeney JA. The role of cerebellar circuitry alterations in the pathophysiology of autism spectrum disorders. Front Neurosci. 2015; 9:296. [PubMed: 26388713]
11. Buckner RL, Krienen FM, Castellanos A, Diaz JC, Yeo BT. The organization of the human cerebellum estimated by intrinsic functional connectivity. J Neurophysiol. 2011; 106:2322–2345. DOI: 10.1152/jn.00339.2011 [PubMed: 21795627]
12. Stoodley CJ, Schmahmann JD. Evidence for topographic organization in the cerebellum of motor control versus cognitive and affective processing. Cortex. 2010; 46:831–844. DOI: 10.1016/j.cortex.2009.11.008 [PubMed: 20152963]
13. Stoodley CJ, Schmahmann JD. Functional topography in the human cerebellum: a meta-analysis of neuroimaging studies. NeuroImage. 2009; 44:489–501. S1053-8119(08)00972-5 [pii]. DOI: 10.1016/j.neuroimage.2008.08.039 [PubMed: 18835452]
14. Strick PL, Dum RP, Fiez JA. Cerebellum and nonmotor function. Ann Rev Neurosci. 2009; 32:413–434. DOI: 10.1146/annurev.neuro.31.060407.125606 [PubMed: 19555291]
15. Grimaldi G, et al. Cerebellar transcranial direct current stimulation (ctDCS): A novel approach to understanding cerebellar function in health and disease. Neuroscientist. 2016; 22:83–97. DOI: 10.1177/1073858414559409 [PubMed: 25406224]
16. De Luca M, Beckmann CF, De Stefano N, Matthews PM, Smith SM. fMRI resting state networks define distinct modes of long-distance interactions in the human brain. NeuroImage. 2006; 29:1359–1367. DOI: 10.1016/j.neuroimage.2005.08.035 [PubMed: 16260155]
17. Deshpande G, Santhanam P, Hu X. Instantaneous and causal connectivity in resting state brain networks derived from functional MRI data. NeuroImage. 2011; 54:1043–1052. DOI: 10.1016/j.neuroimage.2010.09.024 [PubMed: 20850549]
18. Williams JH, et al. Neural mechanisms of imitation and 'mirror neuron' functioning in autistic spectrum disorder. Neuropsychologia. 2006; 44:610–621. DOI: 10.1016/j.neuropsychologia.2005.06.010 [PubMed: 16140346]

19. Clower DM, West RA, Lynch JC, Strick PL. The inferior parietal lobule is the target of output from the superior colliculus, hippocampus, and cerebellum. J Neurosci. 2001; 21:6283–6291. [PubMed: 11487651]
20. Alexander GM, et al. Remote control of neuronal activity in transgenic mice expressing evolved G protein-coupled receptors. Neuron. 2009; 63:27–39. DOI: 10.1016/j.neuron.2009.06.014 [PubMed: 19607790]
21. Armbruster BN, Li X, Pausch MH, Herlitze S, Roth BL. Evolving the lock to fit the key to create a family of G protein-coupled receptors potently activated by an inert ligand. Proc Natl Acad Sci USA. 2007; 104:5163–5168. DOI: 10.1073/pnas.0700293104 [PubMed: 17360345]
22. Arancillo M, White JJ, Lin T, Stay TL, Sillitoe RV. In vivo analysis of Purkinje cell firing properties during postnatal mouse development. J Neurophysiol. 2015; 113:578–591. DOI: 10.1152/jn.00586.2014 [PubMed: 25355961]
23. Peter S, et al. Dysfunctional cerebellar Purkinje cells contribute to autism -like behaviour in Shank2-deficient mice. Nat Commun. 2016; 7:12627. [PubMed: 27581745]
24. Zhou H, et al. Cerebellar modules operate at different frequencies. eLife. 2014; 3:e02536. [PubMed: 24843004]
25. Khan AJ, et al. Cerebro -cerebellar resting-state functional connectivity in children and adolescents with Autism Spectrum Disorder. Biol Psychiatry. 2015; 78:625–34. DOI: 10.1016/j.biopsych.2015.03.024 [PubMed: 25959247]
26. Mesulam MM. From sensation to cognition. Brain. 1998; 121:1013–1052. [PubMed: 9648540]
27. Reep RL, Corwin JV. Posterior parietal cortex as part of a neural network for directed attention in rats. Neurobiol Learn Mem. 2009; 91:104–113. DOI: 10.1016/j.nlm.2008.08.010 [PubMed: 18824116]
28. Clayden JD. Imaging connectivity: MRI and the structural networks of the brain. Funct Neurol. 2013; 28:197–203. DOI: 10.11138/FNeur/2013.28.3.197 [PubMed: 24139656]
29. Lerch JP, et al. Mapping anatomical correlations across cerebral cortex (MACACC) using cortical thickness from MRI. NeuroImage. 2006; 31:993–1003. DOI: 10.1016/j.neuroimage.2006.01.042 [PubMed: 16624590]
30. Asano E, et al. Autism in tuberous sclerosis complex is related to both cortical and subcortical dysfunction. Neurology. 2001; 57:1269–1277. [PubMed: 11591847]
31. Ryu YH, et al. Perfusi on impairments in infantile autism on technetium-99m ethyl cysteinate dimer brain single-photon emission tomography: comparison with findings on magnetic resonance imaging. Eur J Nucl Med. 1999; 26:253–259. [PubMed: 10079316]
32. Moy SS, et al. Social approach in genetically engineered mouse lines relevant to autism. Genes Brain Behav. 2009; 8:129–142. DOI: 10.1111/j.1601-183X.2008.00452.x [PubMed: 19016890]
33. Cupolillo D, et al. Autistic -like traits and cerebellar dysfunction in Purkinje cell PTEN knock-out mice. Neuropsychopharmacology. 2016; 41:1457–1466. DOI: 10.1038/npp.2015.339 [PubMed: 26538449]
34. Reith RM, et al. Loss of Tsc2 in Purkinje cells is associated with autistic -like behavior in a mouse model of tuberous sclerosis complex. Neurobiol Disease. 2013; 51:93–103. DOI: 10.1016/j.nbd.2012.10.014
35. Gottlieb J. From thought to action: the parietal cortex as a bridge between perception, action, and cognition. Neuron. 2007; 53:9–16. DOI: 10.1016/j.neuron.2006.12.009 [PubMed: 17196526]
36. Fogassi L, et al. Parietal lobe: from action organization to intention understanding. Science. 2005; 308:662–667. DOI: 10.1126/science.1106138 [PubMed: 15860620]
37. Marko MK, et al. Behavioural and neural basis of anomalous motor learning in children with autism. Brain. 2015; 138:784–797. DOI: 10.1093/brain/awu394 [PubMed: 25609685]
38. Nebel MB, et al. Intrinsic visual-motor synchrony correlates with social deficits in autism. Biol Psychiatry. 2016; 79:633–641. DOI: 10.1016/j.biopsych.2015.08.029 [PubMed: 26543004]
39. Haswell CC, Izawa J, Dowell LR, Mostofsky SH, Shadmehr R. Representation of internal models of action in the autistic brain. Nat Neurosci. 2009; 12:970–972. DOI: 10.1038/nn.2356 [PubMed: 19578379]
40. Mostofsky SH, et al. Developmental dyspraxia is not limited to imitation in children with autism spectrum disorders. J Int Neuropsychol Soc. 2006; 12:314–326. [PubMed: 16903124]

41. Stoodley CJ, Limperopolous C. Structure-function relationships in the developing cerebellum: Evidence from early-life cerebellar injury and neurodevelopmental disorders. Seminars in Fetal & Neonatal Medicine. 2016; 21:356–364. DOI: 10.1016/j.siny.2016.04.010 [PubMed: 27184461]
42. Van Overwalle F, Baetens K, Marien P, Vandekerckhove M. Social cognition and the cerebellum: Ameta -analysis of over 350 fMRI studies. NeuroImage. 2014; 86:554–572. DOI: 10.1016/j.neuroimage.2013.09.033 [PubMed: 24076206]
43. Jack A, Englander ZA, Morris JP. Subcortical contributions to effective connectivity in brain networks supporting imitation. Neuropsychologia. 2011; 49:3689–3698. DOI: 10.1016/j.neuropsychologia.2011.09.024 [PubMed: 21958651]
44. Jack A, Pelphrey KA. Neural correlates of animacy attribution include neocerebellum in healthy adults. Cereb Cortex. 2015; 25:4240–4247. DOI: 10.1093/cercor/bhu146 [PubMed: 24981794]
45. Deeley Q, et al. An event related functional magnetic resonance imaging study of facial emotion processing in Asperger syndrome. Biol Psychiatry. 2007; 62:207–217. DOI: 10.1016/j.biopsych.2006.09.037 [PubMed: 17400195]
46. LeBlanc JJ, Fagiolini M. Autism: a “critical period” disorder? Neural Plast. 2011; 2011:921680. [PubMed: 21826280]
47. Bryant JL, Boughter JD, Gong S, LeDoux MS, Heck DH. Cerebellar cortical output encodes temporal aspects of rhythmic licking movements and is necessary for normal licking frequency. Eur J Neurosci. 2010; 32:41–52. DOI: 10.1111/j.1460-9568.2010.07244.x [PubMed: 20597972]
48. Boggio PS, Asthana MK, Costa TL, Valasek CA, Osorio AA. Promoting social plasticity in developmental disorders with non-invasive brain stimulation techniques. Front Neurosci. 2015; 9:294. [PubMed: 26388712]
49. Demirtas-Tatlidede A, et al. Safety and proof of principle study of cerebellar vermal theta burst stimulation in refractory schizophrenia. Schizophr Res. 2010; 124:91–100. DOI: 10.1016/j.schres.2010.08.015 [PubMed: 20817483]
50. Amadi U, Ilie A, Johansen-Berg H, Stagg CJ. Polarity-specific effects of motor transcranial direct current stimulation on fMRI resting state networks. NeuroImage. 2014; 88:155–161. DOI: 10.1016/j.neuroimage.2013.11.037 [PubMed: 24287440]
51. Wechsler, D. Wechsler Intelligence Scale for Children. 4. The Psychological Corporation; 2003.
52. Wechsler, D. Wechsler Intelligence Scale for Children. 5. The Psychological Corporation; 2014.
53. Whitfield-Gabrieli S, Nieto-Castanon A. Conn: a functional connectivity toolbox for correlated and anticorrelated brain networks. Brain Connect. 2012; 2:125–141. DOI: 10.1089/brain.2012.0073 [PubMed: 22642651]
54. Behzadi Y, Restom K, Liau J, Liu TT. A component based noise correction method (CompCor) for BOLD and perfusion based fMRI. NeuroImage. 2007; 37:90–101. DOI: 10.1016/j.neuroimage.2007.04.042 [PubMed: 17560126]
55. Muschelli J, et al. Reduction of motion -related artifacts in resting state fMRI using a CompCor. NeuroImage. 2014; 96:22–35. DOI: 10.1016/j.neuroimage.2014.03.028 [PubMed: 24657780]
56. Hollingshead, AB. Four factor index of social status. Yale University Department of Sociology; 1975.
57. Ho DIK, King G, Stuart E. MatchIt: Nonparameteric preprocessing for parametric causal inference. J Stat Softw. 2011; 42:1–28.
58. Stuart EA, Ialongo NS. Matching methods for selection of subjects for follow-up. Multivar Behav Res. 2010; 45:746–765. DOI: 10.1080/00273171.2010.503544
59. Diedrichsen J. A spatially unbiased atlas template of the human cerebellum. NeuroImage. 2006; 33:127–138. DOI: 10.1016/j.neuroimage.2006.05.056 [PubMed: 16904911]
60. Diedrichsen J, Balsters JH, Flavell J, Cussans E, Ramnani N. A probabilistic MR atlas of the human cerebellum. NeuroImage. 2009; 46:39–46. DOI: 10.1016/j.neuroimage.2009.01.045 [PubMed: 19457380]
61. Tzourio-Mazoyer N, et al. Automated anatomical labeling of activations in SPM using a macroscopic anatomical parcellation of the MNI MRI single-subject brain. NeuroImage. 2002; 15:273–289. DOI: 10.1006/nimg.2001.0978 [PubMed: 11771995]

62. Barski JJ, Dethleffsen K, Meyer M. Cre recombinase expression in cerebellar Purkinje cells. Genesis. 2000; 28:93–98. DOI: 10.1002/1526-968X(200011/12)28:3/4<93::AID-GENE10>3.0.CO;2-W [PubMed: 11105049]
63. Kwiatkowski DJ, et al. A mouse model of TSC1 reveals sex-dependent lethality from liver hemangiomas, and up-regulation of p70S6 kinase activity in Tsc1 null cells. Hum Mol Gen. 2002; 11:525–534. [PubMed: 11875047]
64. Márquez-Ruiz J, Cheron G. Sensory stimulation-dependent plasticity in the cerebellar cortex of alert mice. PLoS One. 2012; 7:e36184. [PubMed: 22563448]
65. Quiroga RQ, Reddy L, Kreiman G, Koch C, Fried I. Invariant visual representation by single neurons in the human brain. Nature. 2005; 435:1102–1107. [PubMed: 15973409]
66. Quiroga RQ, Nadasdy Z, Ben-Shaul Y. Unsupervised spike detection and sorting with wavelets and superparamagnetic clustering. Neural Comput. 2004; 16:1661–1687. [PubMed: 15228749]
67. Quiroga RQ. Spike sorting. Curr Biol. 2012; 22:R45–R46. [PubMed: 22280903]
68. Bock NA, Nieman BJ, Bishop JB, Mark Henkelman R. In vivo multiple-mouse MRI at 7 Tesla. Magn ResM ed. 2005; 54:1311–1316. DOI: 10.1002/mrm.20683
69. Lerch JP, et al. Automated cortical thickness measurements from MRI can accurately separate Alzheimer's patients from normal elderly controls. Neurobiol Aging. 2008; 29:23–30. DOI: 10.1016/j.neurobiolaging.2006.09.013 [PubMed: 17097767]
70. Nieman BJ, Flenniken AM, Adamson SL, Henkelman RM, Sled JG. Anatomical phenotyping in the brain and skull of a mutant mouse by magnetic resonance imaging and computed tomography. Physiol Genomics. 2006; 24:154–162. DOI: 10.1152/physiolgenomics.00217.2005 [PubMed: 16410543]
71. Dorr AE, Lerch JP, Spring S, Kabani N, Henkelman RM. High resolution three-dimensional brain atlas using an average magnetic resonance image of 40 adult C57Bl/6J mice. NeuroImage. 2008; 42:60–69. DOI: 10.1016/j.neuroimage.2008.03.037 [PubMed: 18502665]
72. Steadman PE, et al. Genetic effects on cerebellar structure across mouse models of autism using a magnetic resonance imaging atlas. Autism Res. 2014; 7:124–137. DOI: 10.1002/aur.1344 [PubMed: 24151012]
73. Ullmann JF, Watson C, Janke AL, Kurniawan ND, Reutens DC. A segmentation protocol and MRI atlas of the C57BL/6J mouse neocortex. NeuroImage. 2013; 78:196–203. DOI: 10.1016/j.neuroimage.2013.04.008 [PubMed: 23587687]
74. Alexander-Bloch A, Giedd JN, Bullmore E. Imaging structural co-variance between human brain regions. Nat Rev Neurosci. 2013; 14:322–336. DOI: 10.1038/nrn3465 [PubMed: 23531697]
75. Bohbot VD, Lerch J, Thorndycraft B, Iaria G, Zijdenbos AP. Gray matter differences correlate with spontaneous strategies in a human virtual navigation task. J Neurosci. 2007; 27:10078–10083. DOI: 10.1523/JNEUROSCI.1763-07.2007 [PubMed: 17881514]
76. Bozzali M, et al. Anatomical connectivity mapping: a new tool to assess brain disconnection in Alzheimer's disease. NeuroImage. 2011; 54:2045–2051. DOI: 10.1016/j.neuroimage.2010.08.069 [PubMed: 20828625]
77. Evans AC. Networks of anatomical covariance. NeuroImage. 2013; 80:489–504. DOI: 10.1016/j.neuroimage.2013.05.054 [PubMed: 23711536]
78. Kelly C, et al. A convergent functional architecture of the insula emerges across imaging modalities. NeuroImage. 2012; 61:1129–1142. DOI: 10.1016/j.neuroimage.2012.03.021 [PubMed: 22440648]
79. Spreng RN, Turner GR. Structural covariance of the default network in healthy and pathological aging. J Neurosci. 2013; 33:15226–15234. DOI: 10.1523/JNEUROSCI.2261-13.2013 [PubMed: 24048852]
80. Zielinski BA, et al. scMRI reveals large -scale brain network abnormalities in autism. PloS One. 2012; 7:e49172. [PubMed: 23185305]
81. Watson, C.Paxinos, G., Peulles, L., editors. The Mouse Nervous System. 2011.
82. Yang M, Silverman JL, Crawley JN. Automated three-chambered social approach task for mice. Curr Protoc Neurosci. 2011; Chapter 8(Unit 8):26.

83. Yuan E, et al. Graded loss of tuberin in an allelic series of brain models of TSC correlates with survival, and biochemical, histological and behavioral features. Hum Mol Gen. 2012; 21:4286–4300. DOI: 10.1093/hmg/dds262 [PubMed: 22752306]

84. Holmes A, et al. Behavioral characterization of dopamine D5 receptor null mutant mice. Behav Neurosci. 2001; 115:1129–1144. [PubMed: 11584926]

85. Silverman JL, et al. Sociability and motor functions in Shank1 mutant mice. Brain Res. 2011; 1380:120–137. S0006-8993(10)02005-6 [pii]. DOI: 10.1016/j.brainres.2010.09.026 [PubMed: 20868654]

86. Bednar I, et al. Selective nicotinic receptor consequences in APP(SWE) transgenic mice. Mol Cell Neurosci. 2002; 20:354–365. S1044743102911127 [pii]. [PubMed: 12093166]

87. Yang M, Crawley JN. Simple behavioral assessment of mouse olfaction. Curr Protoc Neurosci. 2009; Chapter 8(Unit 8):24.

88. Buitrago MM, Schulz JB, Dichgans J, Luft AR. Short and long-term motor skill learning in an accelerated rotarod training paradigm. Neurobiol Learn Mem. 2004; 81:211–216. DOI: 10.1016/j.nlm.2004.01.001S1074742704000036 [PubMed: 15082022]

89. Hayar A, Bryant JL, Boughter JD, Heck DH. A low-cost solution to measure mouse licking in an electrophysiological setup with a standard analog-to-digital converter. J Neurosci Methods. 2006; 153:203–207. DOI: 10.1016/j.jneumeth.2005.10.023 [PubMed: 16364450]

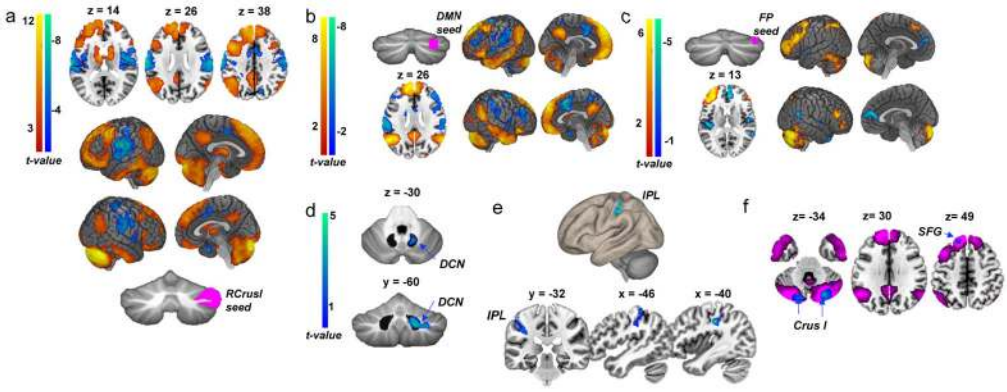


**Fig. 1. FC and BOLD activation before and during tDCS administration in neurotypical adults**

**a**, Pre-tDCS FC from RCrusI seed; correlations are evident with nonmotor regions (red–orange) and anticorrelations with somatomotor regions (blue–green); $n$ =34 individuals. b,**c**, FC from (**b**)Default mode network (DMN) seed and (**c**) Frontoparietal network (FP) seed within RCrusI replicate Buckner et al. [11]. **d**, BOLD signal in the right dentate cerebellar nucleus (DCN; outline of the dentate nucleus is shown) during RCrusI anodal tDCS (anodal< sham; $n$ =18 anodal, $n$ =15 sham; results were thresholded at $P$ <0.001, $k$> 150). **e**, FC between RCrusI and the left IPL during anodal tDCS relative to sham. **f**, FC from the IPL during tDCS (blue; anodal <sham; $n$ =18 anodal, $n$ =15 sham) shown in the context of pre -tDCS DMN network connectivity (fuchsia). SFG, superior frontal gyrus. Results were thresholded at voxel-level $P$ < 0.001, with a false discovery rate (FDR) cluster correction $P$ <0.05.

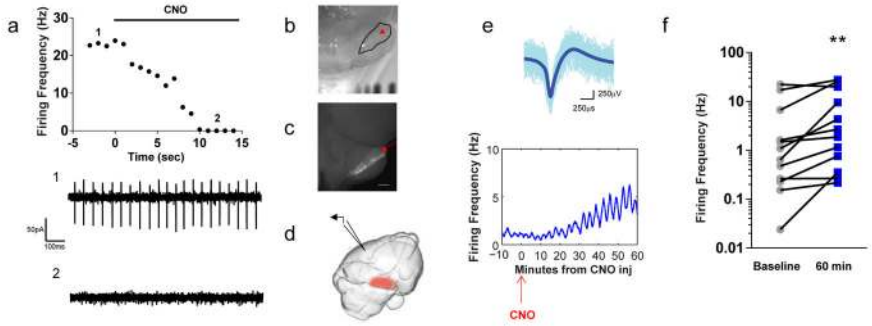


**Fig. 2. Chemogenetically mediated silencing of RCrusI results in increased activity in left parietal association cortex in mice**

**a**, Graphical representation (top) and representative traces (bottom) from extracellular recordings taken from acute slices; simple spike firing rates at (1) baseline and (2) post-CNO administration. **b,c**, Brain showing (**b**) RCrusI and (**c**) fluorescence demonstrating infection of RCrusI (red arrows). Scale bar, 1 mm. **d**, Schematic of in vivo field recordings. RCrusI PNs were infected with AAV8 containing hM4Di (red) while recordings were taken from left parietal association cortices (via electrode, denoted by black wedge) at time of and after CNO administration. **e**, Superimposed single-unit traces (top) with average, summary trace (thick blue line) and time -course of unit firing (bottom). **f**, Summary of all recordings ($n$ =12) in contralateral parietal association cortex with CNO mediated silencing of PNs from RCrusI. $^{**}P < 0.0044$.

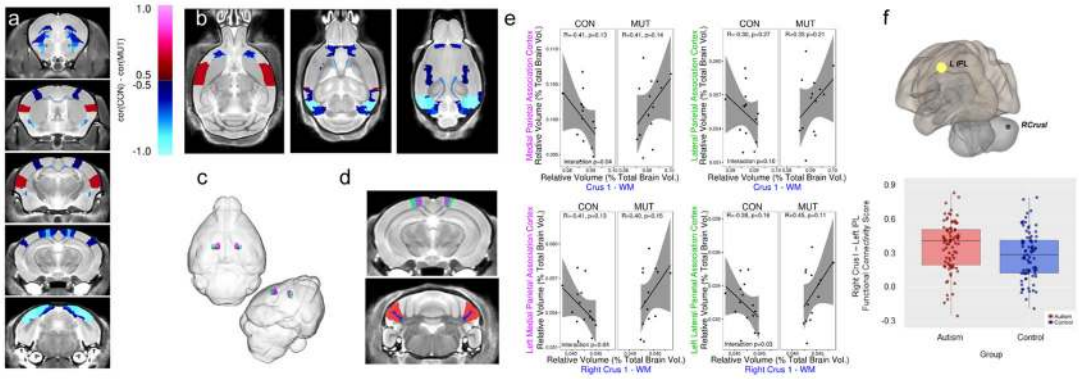


**Fig. 3. Altered connectivity between RCrusI and cortical association areas in ASD mouse model and in individuals with ASD**

**a,b**, Structural connectivity MRI depicting connectivity between CrusI white matter (WM) and cortical association areas in PN *Tsc1*-mutant mice (**a**) coronal sections; (**b**) axial sections. **c**,**d,** Parietal association areas (medial, purple; lateral, green) are highlighted and shown overlying (**c**) the whole brain and (**d**) coronal MRI image. RCrusI highlighted on MRI image (lobule, red; WM, blue). **e**, Correlation plots demonstrating alterations in CrusI–parietal association cortex connectivity. Left, medial; right, lateral parietal association areas with CrusI–WM (top) and RCrusI–WM (bottom). Shaded areas represent 95% confidence intervals. **f**, Functional connectivity between RCrusI and analogous parietal area (IPL) in individuals with ASD ($n$ =81 typically developing control children, $n$ =81 children with autism; $P$= 0.012). Box indicates median and 25th–75th percentiles; whiskers indicate 5th–95th percentiles. CON, control; MUT, mutant.

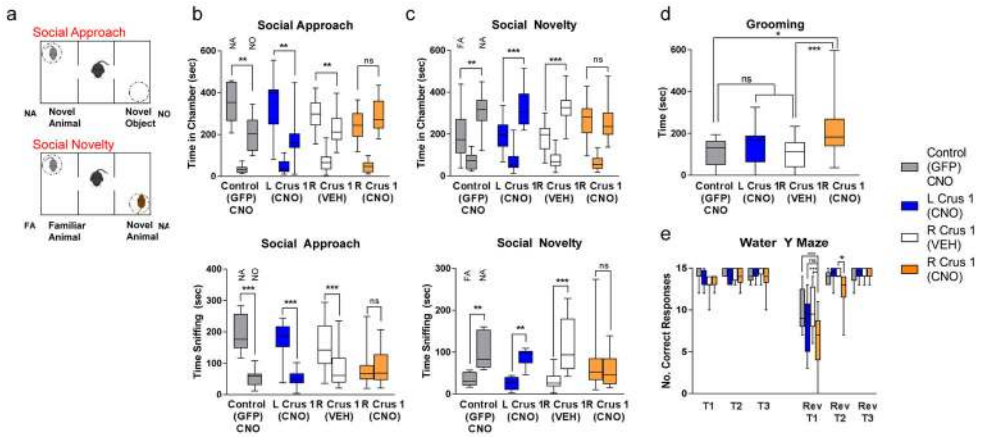


**Fig. 4. Chemogenetic ally mediated inhibition of RCrusI results in autism-related behaviors in mice**

**a**, Schematic of three-chambered apparatus. **b–e**, VEH or CNO treatment of mice harboring AAV8-mediated GFP or hMD4i infection of LCrusI or RCrusI in (**b**) social approach and (**c**) social novelty testing in three -chambered apparatus, shown with time in chamber (top) and time sniffing (bottom), in addition to (**d**) grooming and (**e**) water Y-maze testing ($n = 10$ for each cohort; two-way ANOVA, Bonferroni *post hoc* analysis). Box shows the 25th–75th percentiles; whiskers show 2.5 th–97.5th percentile s. ***$P < 0.001$; ** $P < 0.01$; * $P < 0.05$; ns, not significant; NA, novel animal; NO, novel object; FA, familiar animal; T(1, 2, or 3), timepoint; rev, reversal learning phase. Individual data points for bar graphs plotted in Supplementary Figures 12,13, and 15. Statistical analysis, including $P$ values, and complete animal numbers can be found in Supplementary Table 5.

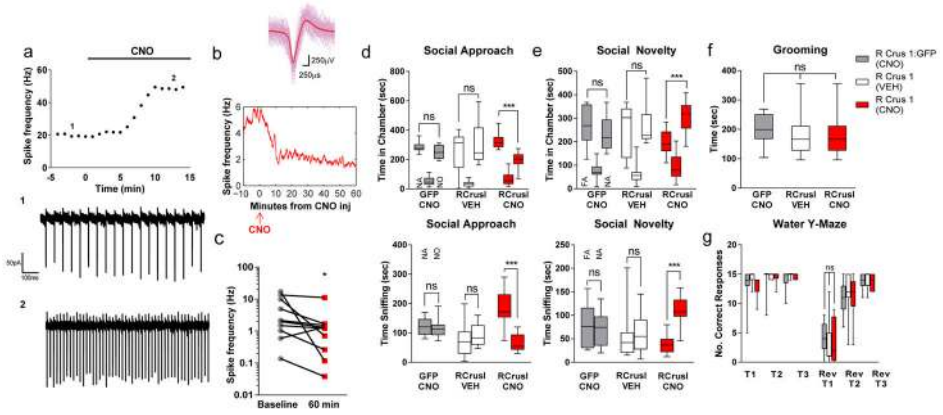


**Fig. 5. Chemogenetically mediated activation of RCrusI rescues social interaction impairment in PN *Tsc1*-mutant mice**

**a**) Representative traces of extracellular recordings from acute slices with AAV8-mediatedhMG3q (DREADD) infection of RCrusI PNs at (i) baseline and after (ii) CNO administration. **b,c**, In vivo field recordings and isolation of single units in parietal association cortex with DREADD-mediated PN activation in RCrusI ($n$ =10, * $P$= 0.0491). $n$ =10 for all cohorts in behavioral testing. **d**–**g**, Social approach (**d**) and social novelty (**e**) testing in three-chambered apparatus shown with time in chamber (top) and time sniffing (bottom), grooming (**f**), and water Y-maze (**g**) upon CNO-mediated activation of RCrusI in PN *Tsc1*-mutant mice (two-way ANOVA, Bonferroni *post hoc* analysis). Box, 25th–75th percentiles; whiskers, 2.5th–97.5th percentile s. ***$P$< 0.001; ns, not significant; NA, novel animal; NO, novel object; FA, familiar animal; T1, trial 1; rev, reversal. Individual data points for bar graphs are plotted in Supplementary Figures 21, 22, and 24. Statistical analysis and complete animal numbers can be found in Supplementary Table 6.